Temporal stability analysis for multiple similarity solutions of viscous incompressible flows in porous channels with moving walls

Sun, Yanxiao; Lin, Ping; Li, Lin

Published in:
Applied Mathematical Modelling

DOI:
10.1016/j.apm.2019.07.056

Publication date:
2020

Temporal stability analysis for multiple similarity solutions of viscous incompressible flows in porous channels with moving walls☆

Yanxiao Sun[1]

Beijing Key Laboratory for Magneto-Photoelectrical Composite and Interface Science, School of Mathematics and Physics, University of Science and Technology Beijing, Beijing 100083, China

Ping Lin[a,], Lin Li[b]*

[a]*Division of Mathematics, University of Dundee, Dundee DD1 4HN, United Kingdom*
[b]*School of Mathematics and Physics, University of South China, Hengyang 421001, China*

Abstract

In this paper, a viscous, incompressible laminar fluid flow along a uniformly porous channel with expanding or contracting walls is considered. We present multiple symmetric steady-state solutions of this flow problem at several different expanding ratios, and use the linear stability theory to analyse the temporal stability for these solutions under symmetric, antisymmetric and general perturbations. We construct second order finite difference schemes for the eigenvalue problems with boundary conditions associated with those perturbations, and observe that most of these solutions which are stable under symmetric perturbations are unstable under antisymmetric perturbations. Furthermore, we verify the linear stability analysis results by directly solving the original perturbed nonlinear time dependent problem, and find that both stability results are consistent.

Keywords: laminar flow, moving walls, expansion ratio, multiple solutions, temporal stability

*Corresponding author
Email address: plin@maths.dundee.ac.uk (Ping Lin)

1. Introduction

We consider multiple solutions of the Navier-Stokes equations for a viscous incompressible fluid flow along a semi-infinite rectangular channel with expanding or contracting porous walls. Such a flow problem has many applications in engineering and biomedicine, such as binary gas diffusion, ablation cooling, phase sublimation, propellant burning, filtration, and the modeling of air circulation in the respiratory system. Many of the exact solutions of the Navier-Stokes equations are obtained for self-similar flows, where equations of motion can be reduced to a nonlinear differential equation and thus the solution process is greatly simplified. These self-similar flow solutions (also called similarity solutions) enhance our understanding of the flow behaviour. However, it is still a question whether these solutions or flow patterns may be observed in reality.

Many authors have calculated the similarity solutions of Navier-Stokes equations for the channel flow with moving walls. Dauenhauer and Majdalani [1] assumed the wall expansion ratio α to be a constant and reduced the Navier-Stokes equations to a boundary value problem of a self-similar fourth order nonlinear ordinary differential equation that was solved by the shooting method. In a later study, asymptotic solutions for this problem were presented by Majdalani *et al.* [2] for small α and small cross-flow Reynolds numbers R and by Majdalani and Zhou [3] for moderate-to-large R. Zhou and Majdalani [4] also provided an exact similarity solution in a slab rocket motor. Recently, Xu *et al.* [5] investigated multiple solutions of the case for which the wall expansion ratio α may be varied from α_0 to α_1 through some given functions, and concluded that the solutions quickly reached the steady state. It is interesting to note that there are multiple or no steady state solutions for some ranges of the cross-flow Reynolds number in this problem. The same phenomenon was also found by Brady and Acrivos [6], who investigated an exact solution to the Navier-Stokes equations for the flow in a channel or tube with an accelerating surface velocity and presented no similarity solutions within the range of $10.25 < R < 147$. Brady and Acrivos [7] later showed the source of the non-existence of similarity

solutions lying in the assumption that the tube is infinite in extent.

Whether a similarity solution represents a real flow depends on the stability of the solution. Therefore, we should not only consider solutions of the fluid flow equations, but also consider their stability.

As for the stability of the similarity solutions of the Navier-Stokes equations in porous channels with stationary walls ($\alpha = 0$), Durlofsky and Brady [8] have studied the spatial stability of a Berman solution under linear symmetric perturbations, and later Ferro and Gnavi [9] extended these results to symmetric and asymmetric solutions under small perturbations. The temporal stability of these flows was examined by Zaturska *et al.* [10]. They proved that most of these flows are temporally unstable to two-dimensional antisymmetric perturbations.

In this paper, we shall focus on the temporal stability of the multiple similarity solutions for symmetric flows in a porous channel with constant wall expansion ratios ($\alpha \neq 0$). The basic equations of the problem are described in Section 2 and the multiple solutions we have discovered at several different expansion ratios α ($-5 \leq \alpha \leq 3$) are shown in Section 3. There exist results for $\alpha = 0$, but the case with $\alpha \neq 0$ is not well studied. So we aim to extend the results from $\alpha = 0$ to $\alpha \neq 0$. The method of our study is numerical, so we have to consider a finite interval including $\alpha = 0$. We simply choose this $[-5, 3]$ as a sample interval for the study. The method generalizes to any value of α. The linear stability analysis of these solutions by numerical means is carried out in Section 4 and verified by directly solving the nonlinear time dependent partial differential equation in Section 5. Finally we conclude in Section 6.

2. Mathematical formulation

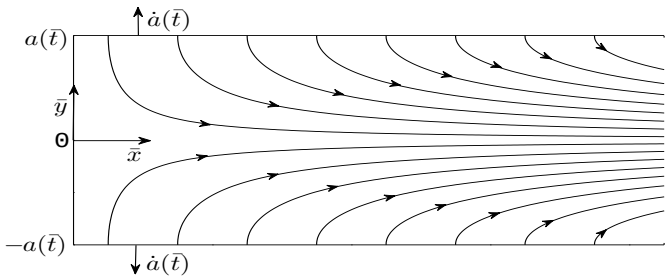

Figure 1: Diagram of the two-dimensional channel with expanding (or contracting) porous walls. The plotted streamlines represent the flow pattern of a symmetric similarity solution of the Navier-Stokes equations.

To begin with, the two-dimensional, viscous, incompressible laminar flow in a porous and rectangular channel is considered. We assume that the height of the channel is $2a$ and the channel length L is unrestricted, one may assume a semi-infinite length, in order to neglect the influence of the opening at the downstream end [11]. Both sidewalls have the same permeability and expand or contract uniformly at a time-dependent rate $\dot{a}$, where $\dot{} = d/d\bar{t}$. The channel is fully open at the downstream end and closed at the head end by an elastic membrane that is allowed to stretch with the longitudinal motion of the channel.

As shown in Fig. 1, a coordinate system with the origin in the center of the channel, the $\bar{x}$-axis parallel to the walls and the $\bar{y}$-axis perpendicular to the walls is chosen. We denote the velocity components in the axial and normal directions by $\bar{u}$ and $\bar{v}$ respectively, and the velocity vector $\bar{\mathbf{v}} = (\bar{u}, \bar{v})$. The over-bar is used to denote dimensional variables. Under these assumptions, the general continuity and motion equations are given as

$$\nabla \cdot \bar{\mathbf{v}} = 0, \tag{1}$$

$$\frac{\partial \bar{\mathbf{v}}}{\partial \bar{t}} + \bar{\mathbf{v}} \cdot \nabla \bar{\mathbf{v}} = -\frac{1}{\rho} \nabla \bar{p} + \nu \triangle \bar{\mathbf{v}}, \tag{2}$$

where ∇ is the gradient operator and $\triangle$ is the Laplace operator, $\bar{p}$, ρ, $\bar{t}$ and ν are the dimensional pressure, density, time and kinematic viscosity, respectively.

Under the stipulation of porous walls, the fluid is injected or aspirated vertically and uniformly through the upper and lower walls of the channel at an absolute velocity v_w that is independent of position. Therefore, consider a symmetric flow field about the midsection plane ($\bar{y} = 0$), that is, the axial and normal velocities $\bar{u}$, $\bar{v}$ are assumed to be an even and odd functions, respectively. Defining the problem in the upper half-domain ($\bar{y} \geq 0$), the necessary boundary conditions can be written as

$$\bar{u}|_{\bar{y}=a} = 0, \quad \bar{v}|_{\bar{y}=a} = -v_w = -A\dot{a}, \tag{3}$$

$$\frac{\partial \bar{u}}{\partial \bar{y}}|_{\bar{y}=0} = 0, \quad \bar{v}|_{\bar{y}=0} = 0, \tag{4}$$

$$\bar{u}|_{\bar{x}=0} = 0. \tag{5}$$

The condition (5) can be achieved by making the flow symmetrical with respect to the plane $\bar{x} = 0$, where $\bar{v}$ is left free.

According to our boundary conditions, we infer that $v_w > 0$ for the case of the injection and $v_w < 0$ for the suction, where $A = v_w/\dot{a}$ is a constant which is a measure of the wall permeability.

As many others do, we introduce the stream function $\bar{\psi}$, and define that

$$\bar{u} = \frac{\partial \bar{\psi}}{\partial \bar{y}}, \quad \bar{v} = -\frac{\partial \bar{\psi}}{\partial \bar{x}}. \tag{6}$$

By taking the curl of both sides of the momentum equation, we obtain the vorticity equation

$$\frac{\partial \bar{\zeta}}{\partial \bar{t}} + \bar{u}\frac{\partial \bar{\zeta}}{\partial \bar{x}} + \bar{v}\frac{\partial \bar{\zeta}}{\partial \bar{y}} = \nu(\frac{\partial^2 \bar{\zeta}}{\partial \bar{x}^2} + \frac{\partial^2 \bar{\zeta}}{\partial \bar{y}^2}), \tag{7}$$

where

$$\bar{\zeta} = \frac{\partial \bar{v}}{\partial \bar{x}} - \frac{\partial \bar{u}}{\partial \bar{y}} = -\Delta \bar{\psi}. \tag{8}$$

Similar to the idea in [3], the following similarity transformation is used:

$$\bar{\psi} = (\nu \bar{x}/a)\bar{f}(\bar{y}, \bar{t}), \tag{9}$$

where $\bar{f}(\bar{y}, \bar{t})$ is independent of the streamwise coordinate. Inserting (9) into (6) and (8), the two velocity components $\bar{u}$, $\bar{v}$ and vorticity $\bar{\zeta}$ can be expressed as

$$\bar{u} = (\frac{\nu \bar{x}}{a})\bar{f}_{\bar{y}}(\bar{y}, \bar{t}), \quad \bar{v} = -(\frac{\nu}{a})\bar{f}(\bar{y}, \bar{t}), \quad \bar{\zeta} = -(\frac{\nu \bar{x}}{a})\bar{f}_{\bar{y}\bar{y}}(\bar{y}, \bar{t}). \tag{10}$$

The boundary condition (5) is found to be satisfied automatically. Upon using (10) into (7), we can obtain a differential equation for $\bar{f}$. That is

$$a^2\bar{f}_{\bar{y}\bar{y}\bar{y}\bar{y}} + \alpha\bar{f}_{\bar{y}\bar{y}} + a\bar{f}\bar{f}_{\bar{y}\bar{y}\bar{y}} - a\bar{f}_{\bar{y}}\bar{f}_{\bar{y}\bar{y}} - a^2\nu^{-1}\bar{f}_{\bar{y}\bar{y}\bar{t}} = 0, \tag{11}$$

where

$$\alpha = \frac{\dot{a}a}{\nu} \tag{12}$$

is the wall expansion ratio. Note that $\alpha > 0$ implies the expansion and $\alpha < 0$ implies the contraction. The boundary conditions for (3) and (4) will be converted to

$$\bar{f}(0) = 0, \quad \bar{f}(a) = R, \quad \bar{f}_{\bar{y}}(a) = 0, \quad \bar{f}_{\bar{y}\bar{y}}(0) = 0, \tag{13}$$

where R is the cross-flow Reynolds number defined by $R = av_w/\nu$ according to references [1-3], [5] and [10], not the Reynolds number usually defined. We can infer that $R > 0$ is for the injection and $R < 0$ for the suction. In the current study, we just consider the case for which R is time invariant, it follows that α is constant and can be specified by its initial value $\dot{a}_0 a_0/\nu$, where a_0 and $\dot{a}_0$ are the initial channel half-height and expansion rate, respectively. Integrating (12), the channel height of the present similarity solution will vary in time according to $a = \sqrt{a_0^2 + 2\nu\alpha\bar{t}}$.

Next, we introduce the following scalings:

$$\psi = \frac{\bar{\psi}}{av_w}, \quad u = \frac{\bar{u}}{v_w}, \quad v = \frac{\bar{v}}{v_w}, \quad x = \frac{\bar{x}}{a}, \quad y = \frac{\bar{y}}{a}, \quad f = \frac{\bar{f}}{R}, \quad t = \frac{v_w\bar{t}}{a}, \tag{14}$$

then the dimensionless equations for (9),(11) and (13) can be written as

$$\psi = xf(y,t), \tag{15}$$

$$(1 - \frac{2\alpha t}{R})f_{yyt} - \frac{1}{R}f_{yyyy} - ff_{yyy} + f_y f_{yy} - \frac{\alpha}{R}(yf_{yyy} + 3f_{yy}) = 0, \tag{16}$$

$$f(0) = 0, \quad f(1) = 1, \quad f_y(1) = 0, \quad f_{yy}(0) = 0, \tag{17}$$

and so

$$u = xf_y, \quad v = -f. \tag{18}$$

In particular, when $f_{yyt} = 0$, there are steady solutions with

$$\psi = xF(y), \tag{19}$$

where F satisfies the following equation

$$F'''' + R(FF''' - F'F'') + \alpha(yF''' + 3F'') = 0 \tag{20}$$

and the boundary conditions

$$F(0) = 0, \quad F(1) = 1, \quad F'(1) = 0, \quad F''(0) = 0. \tag{21}$$

Here a prime denotes differentiation with respect to y. Particularly, equation (20) is Berman's classic equation in [12] when $\alpha = 0$.

3. Multiple solutions of the steady-state problem

The numerical solution of (20), subject to boundary conditions (21), is a two-point boundary value problem, and the numerical results of above problem will be influenced by the parameters α and R. We calculate these multiple solutions by MATLAB's function BVP4c and show the results by drawing graphs of the variable $-F''(1)$ with R at different values of α ($-5 \leq \alpha \leq 3$). The method of judging multiple solutions by plotting $-F''(1)$ versus R has been used in many past studies. This quantity is proportional to the skin friction at the wall. There is no rigorous proof that different solutions must have different $F''(1)$, but from computations of our own and other researchers, different $F''(1)$ indicates different solutions. We only need these solutions for the stability analysis later.

The numerical solutions at $\alpha = 0$, $\pm 1/2$, ± 1, ± 2, ± 3 and -5 that we have discovered are plotted in Figs. 2 and 3. In each case of $-5 \leq \alpha \leq 2$, the solution curves have been labelled I, II and III, indicating three different types of solutions: type I is in $-\infty < R < \infty$ on the lowest branch; type II (on the lower branch) and type III (on the upper branch) exist in a common semi-infinite domain, spanning over $-\infty < R < R_\alpha$, where R_α is the critical cross-flow Reynolds number for the corresponding α. According to our numerical

method, $R_{-5} = -14.486$, $R_{-3} = -13.918$, $R_{-2} = -13.482$, $R_{-1} = -12.909$, $R_{-1/2} = -12.561$, $R_0 = -12.165$, $R_{1/2} = -11.724$, $R_1 = -11.245$ and $R_2 = -10.295$. Particularly, the results for $\alpha = 0$ are in good agreement with those presented by Zaturska *et al.* [10]. When $\alpha = 3$, as shown in Fig. 3, a new type of solutions emerges which is marked as IV, while other types of solutions, similar to the classification for $-5 \leq \alpha \leq 2$, are marked as I, II and III: type I is in $R_3^1 < R < \infty$ and type IV is in $R_3^1 < R < -0.796$; types II and III exist in a common semi-infinite domain, spanning over $-\infty < R < R_3^2$, where $R_3^1 = -4.25$ and $R_3^2 = -9.545$ are the critical cross-flow Reynolds numbers for types I, IV and types II, III, respectively. Moreover, no solution is found for $R_3^2 < R < R_3^1$. Additionally, at a fixed R, the wall friction increases as the contraction ratio $|\alpha|$ is increased as shown in Fig. 2, and decreases as the expansion ratio α is increased for types II and III as shown in Fig. 3. We will only consider the above solutions, although there may be other solutions in all R.

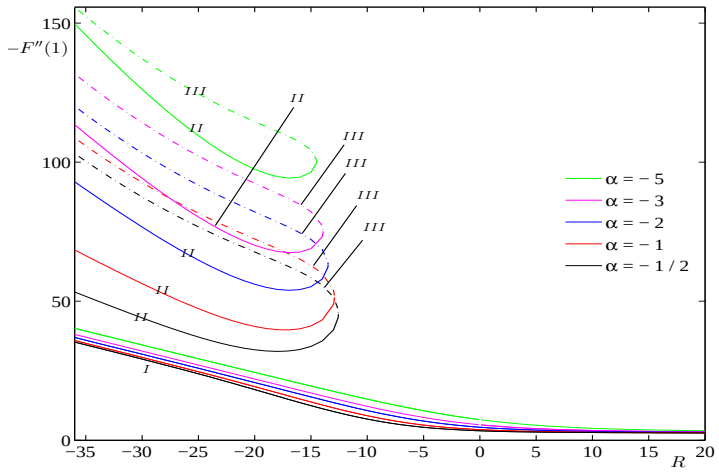

Figure 2: Values of $-F''(1)$ versus R for the types I, II, and III symmetric solutions over some values of α ($-5 \leq \alpha \leq -1/2$). To make it easier to distinguish, the solutions of types II and III at the same α are drawn with solid and chain lines of the same color, respectively.

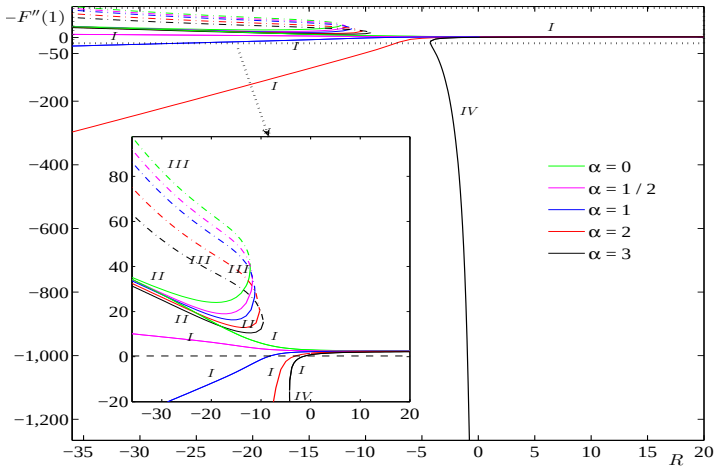

Figure 3: Values of $-F''(1)$ versus R for the types I, II, III and IV symmetric solutions over some values of α ($0 \leq \alpha \leq 3$). To make it easier to distinguish, similarly, the solutions of types II and III at the same α are drawn with solid and chain lines of the same color, respectively.

The characteristics of these four types of solutions are as follows:

(1) Type I covers the solutions whose axial velocity profiles have a maximum at the center of the channel.

(2) Type II includes the solutions whose axial velocity profiles have an inflection point and a maximum between the center of the channel and the wall and whose centerline velocity is positive for sufficiently large negative values of R.

(3) Type III contains axial velocity profiles with the same form as type II solutions but with reverse flow at the center of the channel.

(4) Type IV includes the solutions which have reverse flow near the wall of the channel and for which $F''(1) > 0$.

Figs. 4 and 5 demonstrate the axial velocity profiles $F'(y)$ for type I solutions at low, moderate and high injection and suction cross-flow Reynolds numbers within a range of wall expansion ratios. In all cases of α, the profiles have a maximum at the centerline. For $R > 0$ (injection), they monotonically decrease to 0 at the wall, and the velocity at the centerline ($u(0)/x$) is approximately

equal to 1.57 as $R \to \infty$. For $R < 0$ (suction), the profiles represent a continuous deformation from those for $R > 0$. When the expansion ratio $\alpha \leq 0$, as $R \to -\infty$, they are approximately equal to 1 everywhere except in a thin boundary layer forming above the wall. Furthermore, the boundary layer becomes thinner with the decrease of R. The profiles with $\alpha = 1/2$ keep monotonically decreasing which have a centerline velocity approximately equal to 1.4317 as $R \to -\infty$. When $\alpha \geq 1$, the profiles are no longer monotonic below a sufficiently large negative value of R which depends on the corresponding α. Instead, they pass through a negative minimum before going to 0 at the wall, that is clearly shown in Figs. 5(b) and 5(c), which indicates reverse flow occurs near the wall of the channel. This phenomenon can also be seen in Fig. 3, in the case of $\alpha = 1$ or 2, as R decreases, the value of $-F''(1)$ vanishes at a particular R and then becomes negative, which means the wall friction decreases until it changes direction.

The axial velocity profiles for type II solutions at some suction cross-flow Reynolds numbers are described in Fig. 6. For each case of α, it can be seen that they are characterized by a point of inflection and a maximum between the centerline and the wall of the channel. When the expansion ratio $\alpha \leq -1$, little change occurs in the profiles, with the sign of the centerline velocity changing from negative to positive as R decreases, which means the reverse flow at the centerline disappears. When the expansion ratio $\alpha \geq 0$ and $R \to -\infty$, the velocity is close to 1 everywhere except in a boundary layer, which is similar to that described for type I solutions with $\alpha \leq 0$.

Fig. 7 presents the axial velocity profiles for type III solutions that occur at some suction cross-flow Reynolds numbers. For all α, these profiles have the same shape as those of type II, except that there is a region of reverse flow near the center of the channel at any R where these solutions exist.

The velocity profiles for four types of solutions at $\alpha = 3$ over some suction cross-flow Reynolds numbers are shown in Fig. 8. For the types I, II and III solutions, they have the similar characteristics with those solutions at $\alpha = 2$, respectively, so we will not repeat it here. For the type IV solutions, the profiles are characterized by a rapid increase in the centerline velocity and the wall

velocity gradient ($F''(1)$) as R increases, and the development of reverse flow near the wall of the channel.

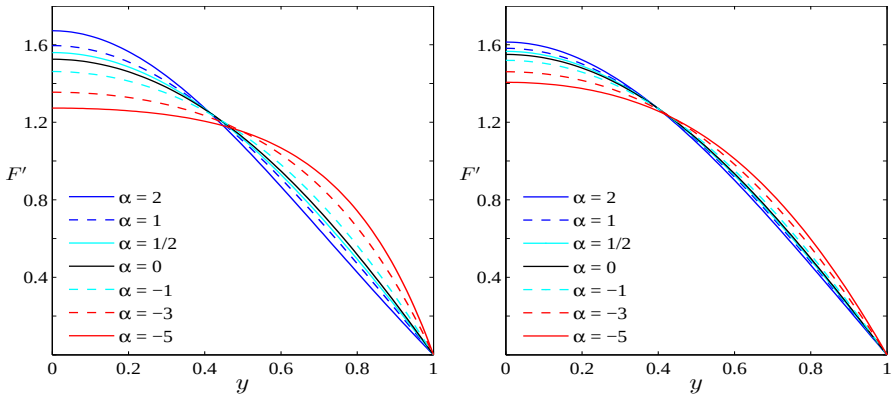

(a) $R = 5$ (b) $R = 20$

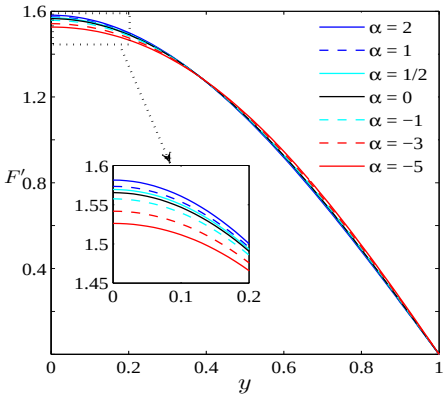

(c) $R = 100$

Figure 4: Axial velocity profiles $F'(y)$ for type I solutions over a range of wall expansion ratios α and an injection cross-flow Reynolds number of (a) $R = 5$, (b) $R = 20$ and (c) $R = 100$.

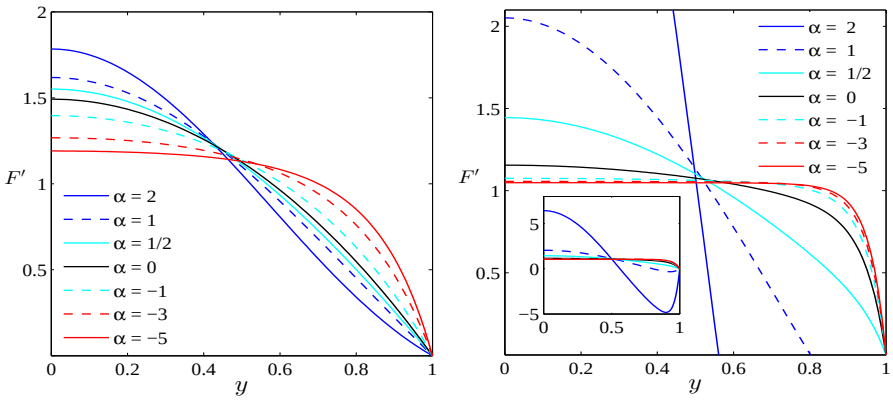

(a) $R = -1$ (b) $R = -20$

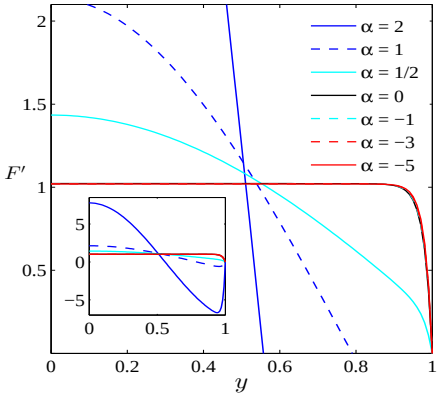

(c) $R = -50$

Figure 5: Axial velocity profiles $F'(y)$ for type I solutions over a range of wall expansion ratios α and a suction cross-flow Reynolds number of (a) $R = -1$, (b) $R = -20$ and (c) $R = -50$.

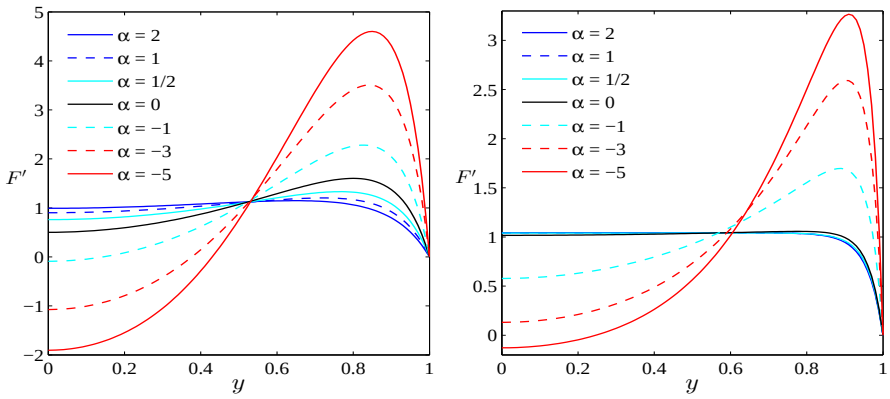

(a) $R = -15$ (b) $R = -30$

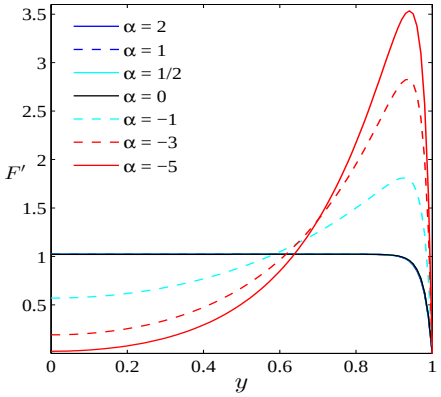

(c) $R = -50$

Figure 6: Axial velocity profiles $F'(y)$ for type II solutions over a range of wall expansion ratios α and a suction cross-flow Reynolds number of (a) $R = -15$, (b) $R = -30$ and (c) $R = -50$.

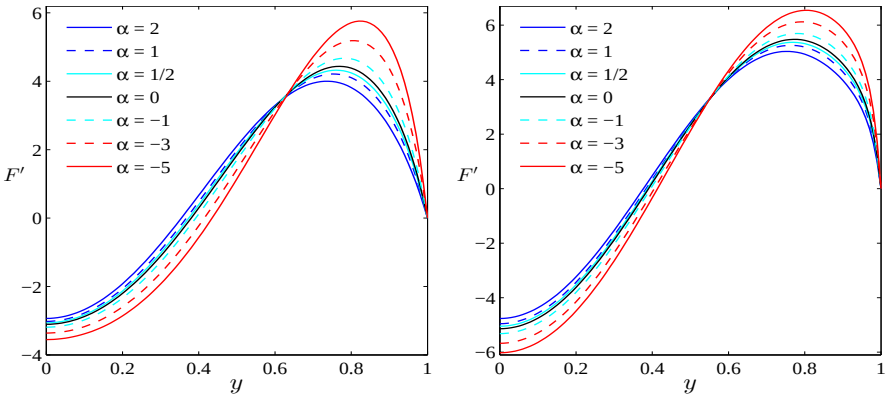

(a) $R = -15$ (b) $R = -50$

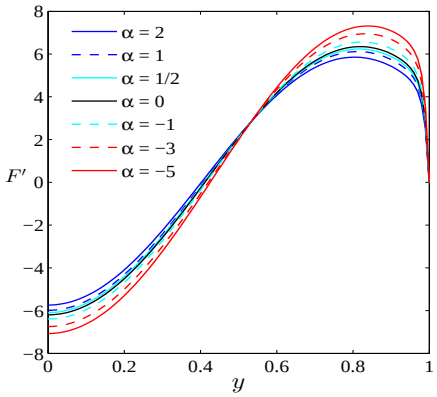

(c) $R = -100$

Figure 7: Axial velocity profiles $F'(y)$ for type III solutions over a range of wall expansion ratios α and a suction cross-flow Reynolds number of (a) $R = -15$, (b) $R = -50$ and (c) $R = -100$.

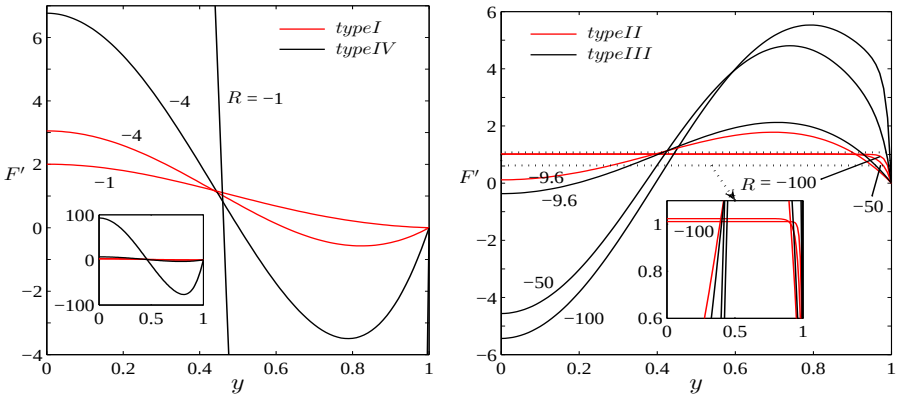

(a) $R = -1, -4$ (b) $R = -9.6, -50, -100$

Figure 8: Axial velocity profiles $F'(y)$ for solutions of (a) types I and IV over $R = -1, -4$ and (b) types II and III over $R = -9.6, -50, -100$; $\alpha = 3$.

4. Temporal stability analysis

We have observed multiple solutions for this steady flow problem. Physically we want to know whether these basic flows can be observed or not. If one of the flows is disturbed slightly, will the disturbance die away and the flow return to its original laminar state, or grow so much that the basic flow becomes a different laminar or a turbulent flow? This can be answered with a linear stability analysis of these solutions.

To determine the linear temporal stability of above solutions, we let

$$f(y,t) = F(y) + g(y,t), \tag{22}$$

linearize (16) for small g, and consider perturbations of the forms

$$\begin{cases} g(y,t) = e^{st}G(y) & (\alpha = 0) \\ g(y,t) = (1 - \dfrac{2\alpha t}{R})^{-s}G(y) & (\alpha < 0) \\ g(y,t) = (1 - \dfrac{2\alpha t}{R})^{s}G(y) & (\alpha > 0) \end{cases} \tag{23}$$

which are obtained by the method of separation of variables. This leads to the

following eigenvalue problems:

$$\begin{cases} G'''' + R(FG''' + F'''G - F'G'' - F''G') + \alpha(yG''' + 3G'') \\ = RsG'' \qquad\qquad (\alpha = 0) \\ G'''' + R(FG''' + F'''G - F'G'' - F''G') + \alpha(yG''' + 3G'') \\ = 2\alpha sG'' \qquad\qquad (\alpha < 0) \\ G'''' + R(FG''' + F'''G - F'G'' - F''G') + \alpha(yG''' + 3G'') \\ = -2\alpha sG'' \qquad\qquad (\alpha > 0) \end{cases} \tag{24}$$

associated with the homogeneous boundary conditions of symmetric perturbations

$$G(0) = 0, \quad G(1) = 0, \quad G'(1) = 0, \quad G''(0) = 0 \tag{25}$$

and the boundary conditions of antisymmetric perturbations

$$G'(0) = 0, \quad G(1) = 0, \quad G'(1) = 0, \quad G'''(0) = 0 \tag{26}$$

in the half-channel domain $y \in [0, 1]$, or associated with the boundary conditions of general perturbations in the whole channel ($y \in [-1, 1]$)

$$G(-1) = 0, \quad G(1) = 0, \quad G'(-1) = 0, \quad G'(1) = 0. \tag{27}$$

In the eigenvalue problem (24) with respect to (27), F is the symmetric solution of the steady-state problem (20) with the boundary conditions

$$F(-1) = -1, \quad F(1) = 1, \quad F'(-1) = 0, \quad F'(1) = 0. \tag{28}$$

Here, we assume that the three sets of eigenfunctions G are complete, so that the development of an arbitrary symmetric, antisymmetric or general initial perturbation can be represented, otherwise, only a special type of perturbations linearly combined by eigenfunctions are analysed. The stability results here will be verified later.

For a given cross-flow Reynolds number R and expansion ratio α, the dimensionless transformation $t = v_w\bar{t}/a = R\nu\bar{t}/a^2 = R\nu\bar{t}/(a_0^2 + 2\nu\alpha\bar{t})$. Together with (23), both the sign of the real part of the eigenvalue s ($Re(s)$) and the

value of t will determine the stability of a given flow F. When $\alpha = 0$, for $R > 0$, the instability is implied if there is an eigenvalue such that $Re(s) > 0$. For $R < 0$, the sign of t becomes negative. In this case, the instability is implied if there is an eigenvalue such that $Re(s) < 0$. When $\alpha < 0$ (for contraction), the instability is implied if there is an eigenvalue such that $Re(s) < 0$. When $\alpha > 0$ (for expansion), we note that t is finite, and when $t \to (R/2\alpha)$, the channel height a has already reached infinity. Therefore the instability in $\alpha > 0$ occurs at $t \to (R/2\alpha)$ and $Re(s) < 0$ for at least one eigenvalue.

4.1. Symmetric perturbations

Given a similarity solution F at a certain R and α, we have taken a second order finite difference scheme for the eigenvalue problem (24) ($\alpha = 0$) associated with the boundary conditions (25):

$$\begin{aligned}
&\frac{G_{j+2}-4G_{j+1}+6G_j-4G_{j-1}+G_{j-2}}{h^4}+R(F_j\frac{\frac{1}{2}G_{j+2}-G_{j+1}+G_{j-1}-\frac{1}{2}G_{j-2}}{h^3}\\
&+F_j'''G_j-F_j'\frac{G_{j+1}-2G_j+G_{j-1}}{h^2}-F_j''\frac{G_{j+1}-G_{j-1}}{2h})\\
&+\alpha(jh\frac{\frac{1}{2}G_{j+2}-G_{j+1}+G_{j-1}-\frac{1}{2}G_{j-2}}{h^3}+3\frac{G_{j+1}-2G_j+G_{j-1}}{h^2})\\
&=Rs\frac{G_{j+1}-2G_j+G_{j-1}}{h^2}, \qquad\qquad j=2,\cdots,M-2,
\end{aligned} \tag{29}$$

$$\begin{aligned}
&G_0=0, \quad G_M=0,\\
&\frac{\frac{137}{60}G_M-5G_{M-1}+5G_{M-2}-\frac{10}{3}G_{M-3}+\frac{5}{4}G_{M-4}-\frac{1}{5}G_{M-5}}{h}=0,\\
&\frac{-\frac{5}{6}G_5+\frac{61}{12}G_4-13G_3+\frac{107}{6}G_2-\frac{77}{6}G_1+\frac{15}{4}G_0}{h^2}=0,
\end{aligned} \tag{30}$$

where h is the increment of the variable y, F_j and G_j are the approximations to $F(jh)$ and $G(jh)$, respectively. Similar finite difference schemes have been constructed for the eigenvalue problems for other α. We need to solve G_1 and G_{M-1} from (30) and insert G_1 into (29) when $j = 2, 3$, and insert G_{M-1} into (29) when $j = M-3, M-2$. Then we can obtain a system of equations $A\mathbf{G} = s\mathbf{G}$, where A is a matrix and $\mathbf{G} = (G_2, G_3, \cdots, G_{M-3}, G_{M-2})$, and obtain s by solving the eigenvalues of A.

For the problem (24) subject to the (25), we mark the minimum real part of its eigenvalues as r in the case of $\alpha \neq 0$. When $\alpha = 0$, r represents the maximal real part for $R > 0$ and the minimum real part for $R < 0$. r is plotted with R in Figs. 9-11.

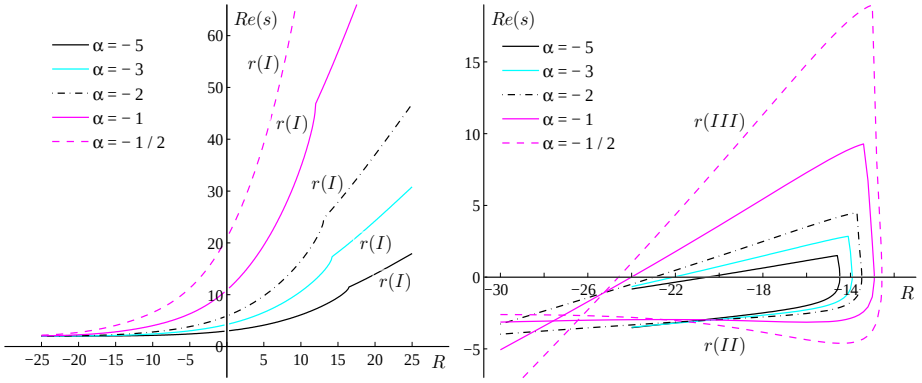

Figure 9: Real part (r) of the eigenvalues for (a) type I and (b) types II and III symmetric solutions with various values of α ($-5 \leq \alpha \leq -1/2$) under symmetric perturbations.

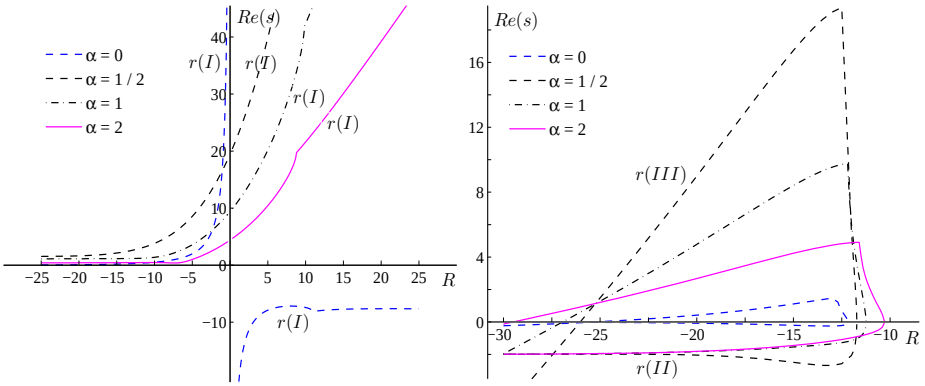

Figure 10: Real part (r) of the eigenvalues for (a) type I and (b) types II and III symmetric solutions with various values of α ($0 \leq \alpha \leq 2$) under symmetric perturbations.

Table 1: The stability ranges of R of type III solutions with various values of α ($-5 \leq \alpha \leq 2$) under symmetric perturbations.

α	stability ranges of R	α	stability ranges of R	α	stability ranges of R
-5	(-20.54821, R_{-5})	-1	(-24.01060, R_{-1})	1/2	(-26.03318, $R_{1/2}$)
-3	(-22.08950, R_{-3})	-1/2	(-24.60257, $R_{-1/2}$)	1	(-26.93949, R_1)
-2	(-22.98086, R_{-2})	0	(-25.26794, R_0)	2	(-29.50348, R_2)

As shown in Figs. 9 and 10, when $-5 \leq \alpha \leq 2$ and $\alpha \neq 0$, for type I solutions, we can obtain that $Re(s)$ are all positive for $-\infty < R < \infty$. When $\alpha = 0$, for type I solutions, we can obtain that $Re(s)$ are all negative for $R > 0$ (injection) and positive for $R < 0$ (suction). Furthermore, $r \to 0$ as $R \to -\infty$ under this circumstance. Therefore, type I solutions with $-5 \leq \alpha \leq 2$ are always stable for $-\infty < R < \infty$. For type II solutions, r is negative for $-\infty < R < R_i$ with $\alpha = i$ ($i = 0$, $\pm 1/2$, ± 1, ± 2, -3 and -5), so the type II solutions with $-5 \leq \alpha \leq 2$ are always unstable. For type III solutions of each case of $-5 \leq \alpha \leq 2$, there is a region of R where only positive $Re(s)$ are found, and the sign of r changes as R decreases through a particular value, indicating that the solutions begin to be unstable. The stability ranges of R of type III solutions with $\alpha = i$ ($i = 0$, $\pm 1/2$, ± 1, ± 2, -3 and -5) are shown in Table 1, and we can observe that the stable regions are getting bigger and bigger with the increase of α. Particularly, the stability results at $\alpha = 0$ are consistent with those of Zaturska *et al.* [10].

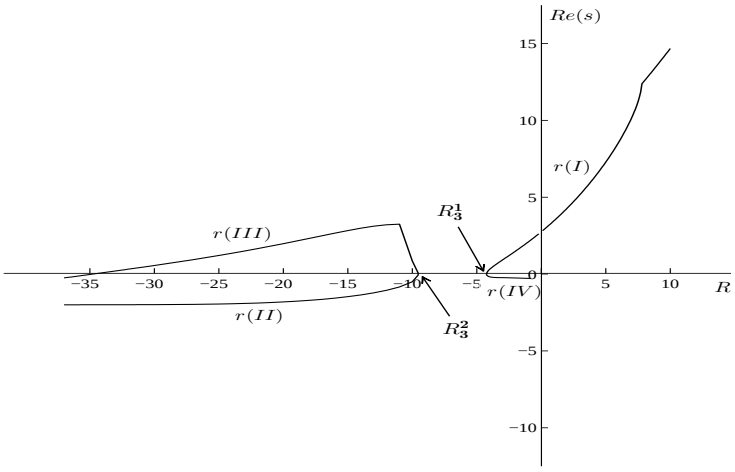

Figure 11: Real part (r) of the eigenvalues for types I, II, III and IV symmetric solutions with $\alpha = 3$ under symmetric perturbations.

When $\alpha = 3$, the stability results are shown in Fig. 11, where type I solutions are stable for $R_3^1 < R < \infty$; type IV solutions are unstable for $R_3^1 < R < -0.796$, since r is negative in this range; similarly, type II solutions are unstable for $-\infty < R < R_3^2$; for type III solutions, the sign change of r as R decreases through the value -34.77574 heralds the onset of their instability. So type III solutions are temporally stable only for $-34.77574 < R < R_3^2$.

4.2. Antisymmetric perturbations

For symmetric perturbations with boundary conditions given by (25), we have found that type I solutions with $-5 \leq \alpha \leq 3$ are all stable at the R where they exist, type III solutions with $-5 \leq \alpha \leq 3$ are stable in small regions of R. However, when we use the conditions (26), the perturbations are antisymmetric. We obtain the eigenvalues according to the problem (24) subject to the (26) by a similar finite difference method given earlier. The real part p is plotted vs R in Figs. 12-14, where p represents the minimum real part of the eigenvalues s in the case of $\alpha \neq 0$. When $\alpha = 0$, p represents the minimum real part of the eigenvalues s for $R < 0$, and the maximal real part of s for $R > 0$.

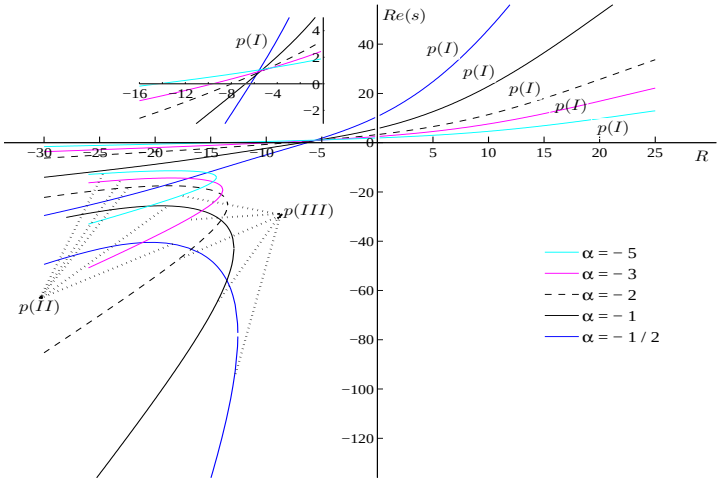

Figure 12: Real part (p) of the eigenvalues for types I, II and III symmetric solutions with various values of α ($-5 \leq \alpha \leq -1/2$) under antisymmetric perturbations.

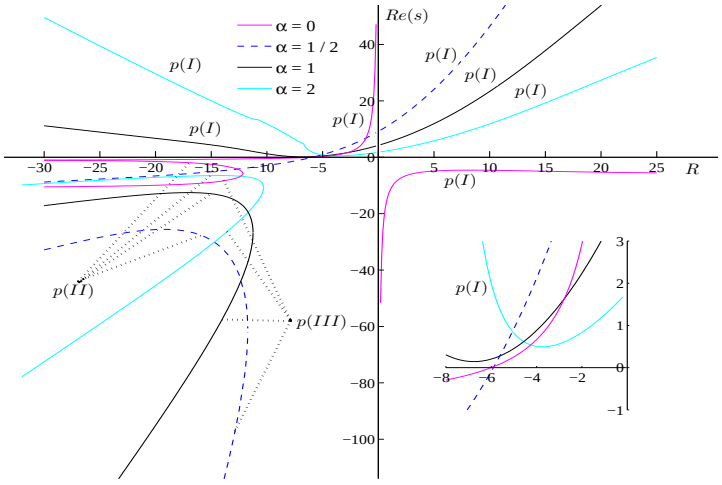

Figure 13: Real part (p) of the eigenvalues for types I, II and III symmetric solutions with various values of α ($0 \leq \alpha \leq 2$) under antisymmetric perturbations.

Table 2: The stability ranges of R of type I solutions with various values of α ($-5 \leq \alpha \leq 2$) under antisymmetric perturbations.

α	stability ranges of R	α	stability ranges of R	α	stability ranges of R
-5	(-14.315,∞)	-1	(-6.759,∞)	1/2	(-5.904,∞)
-3	(-9.605,∞)	-1/2	(-6.317,∞)	1	($-\infty$,∞)
-2	(-7.961,∞)	0	(-6.001,∞)	2	($-\infty$,∞)

In Figs. 12 and 13, for type I solutions with $-5 \leq \alpha \leq 2$, only positive real part of the eigenvalues exist for $R > 0$ when $\alpha \neq 0$, and only negative $Re(s)$ exist for $R > 0$ when $\alpha = 0$, namely the injection flows are always stable. However, for $R < 0$ (suction), the stability of type I solutions varies for different α. As shown in Figs. 12 and 13, for each case of $-5 \leq \alpha \leq 1/2$, the branch p crosses the line $Re(s) = 0$ at a particular value of R shown in Table 2, and then the value of p becomes negative below this cross-flow Reynolds number, which indicates that the suction flows lose their temporal stability. Furthermore, $p \to -1$ as $R \to -\infty$ when $\alpha = 0$. For the cases of $1 \leq \alpha \leq 2$, $Re(s)$ for type I solutions are all positive for $R < 0$, thus the type I solutions with $1 \leq \alpha \leq 2$ are always stable. The stability ranges of R of type I solutions with $\alpha = i$ ($i = 0$, $\pm 1/2$, ± 1, ± 2, -3 and -5) are shown in Table 2. For type II or III solutions with $-5 \leq \alpha \leq 2$, in Figs. 12 and 13, p is negative for $-\infty < R < R_i$ with $\alpha = i$ ($i = 0$, $\pm 1/2$, ± 1, ± 2, -3 and -5) and, further, $p \to -1$ as $R \to -\infty$ for the type II solutions with $\alpha = 0$, so that the types II and III solutions with $-5 \leq \alpha \leq 2$ are always unstable.

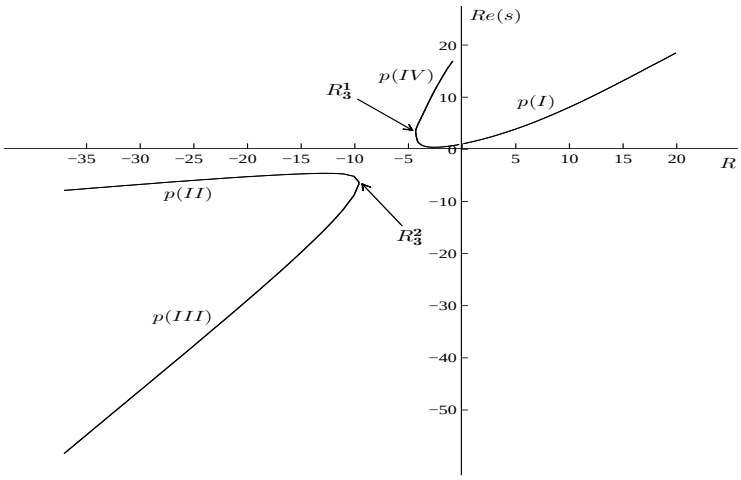

Figure 14: Real part (p) of the eigenvalues for types I, II, III and IV symmetric solutions with $\alpha = 3$ under antisymmetric perturbations.

When $\alpha = 3$, in Fig. 14, $Re(s)$ for type I solutions are all positive for $R_3^1 < R < \infty$, so the type I solutions are stable. Similarly, the type IV solutions are also stable. p for types II and III solutions are always negative for $R < R_3^2$, so the solutions of types II and III are always unstable for $-\infty < R < R_3^2$.

4.3. General perturbations

We have gained the stability results of symmetric solutions under symmetric perturbations and antisymmetric perturbations. Now we consider $y \in [-1, 1]$ and use the boundary conditions (27), where all types of perturbations in the interval $y \in [-1, 1]$ are included in the analysis. Proceeding as in the previous section, we obtain the eigenvalues according to the problem (24) associated with (27) by a similar finite difference method given earlier and show the real part q in Figs. 15-17, where q represents the minimum real part of the eigenvalues s in the case of $\alpha \neq 0$. When $\alpha = 0$, q represents the minimum real part of the eigenvalues s for $R < 0$, and the maximal real part of s for $R > 0$.

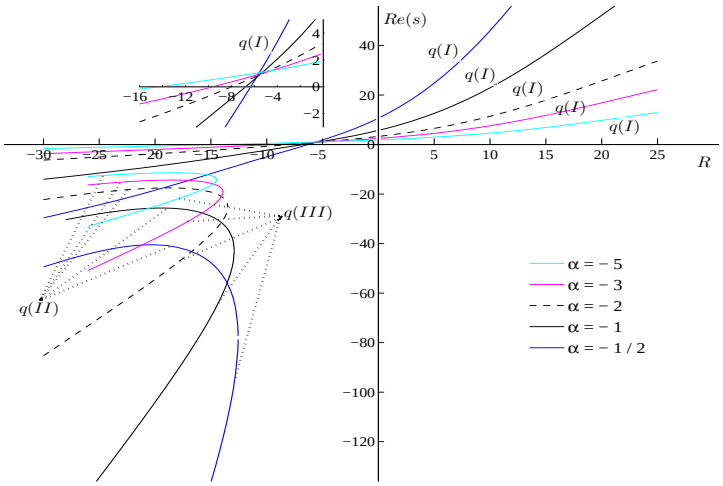

Figure 15: Real part (q) of the eigenvalues for types I, II and III symmetric solutions with various values of α ($-5 \leq \alpha \leq -1/2$) under perturbations in the interval $y \in [-1, 1]$.

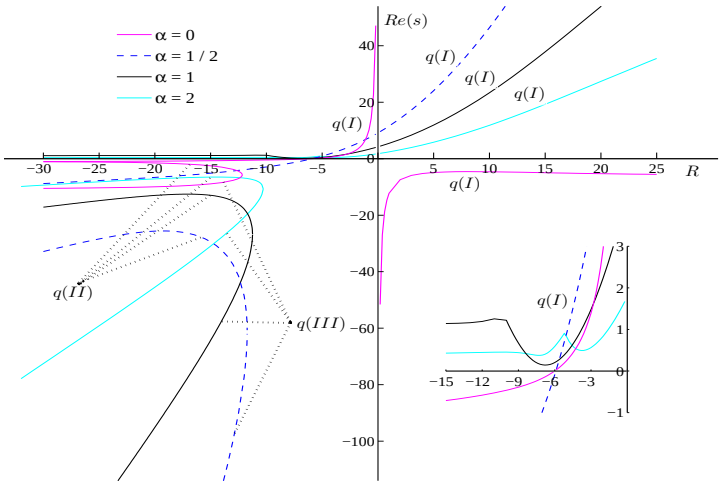

Figure 16: Real part (q) of the eigenvalues for types I, II and III symmetric solutions with various values of α ($0 \leq \alpha \leq 2$) under perturbations in the interval $y \in [-1, 1]$.

In Figs. 15 and 16, the stability ranges of R for type I solutions with $\alpha = i$ ($i = 0, \pm 1/2, \pm 1, \pm 2, -3$ and -5) under general perturbations are the same as those under antisymmetric perturbations, and have been given in Table 2. For type II or III solutions, in Figs. 15 and 16, q is negative for $-\infty < R < R_i$ with

$\alpha = i$ ($i = 0$, $\pm 1/2$, ± 1, ± 2, -3 and -5), so that the types II and III solutions with $-5 \leq \alpha \leq 2$ are always unstable.

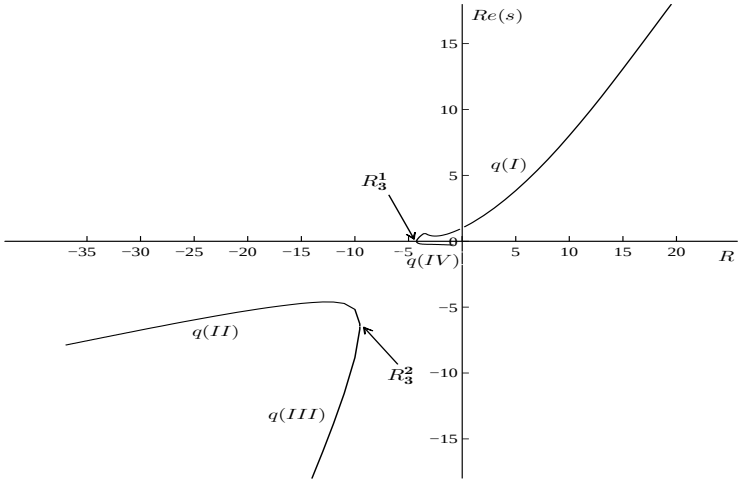

Figure 17: Real part (q) of the eigenvalues for types I, II, III and IV symmetric solutions with $\alpha = 3$ under perturbations in the interval $y \in [-1, 1]$.

When $\alpha = 3$, in Fig. 17, similarly, the type I solutions are stable for $R_3^1 < R < \infty$, and the type IV solutions are unstable for $R_3^1 < R < -0.796$, types II and III solutions are always unstable for $-\infty < R < R_3^2$.

Consequently, the linear temporal stability of symmetric solutions seems to be determined by the eigenvalues obtained under symmetric and antisymmetric perturbations. When $-5 \leq \alpha \leq 3$, the type I solutions are stable in some ranges of R. However, the other types of solutions whose axial velocity profiles have an inflection point are always unstable, thus these solutions may not be physically meaningful and consequently are not expected to be observed in engineering applications.

5. The verification of the stability results

We have provided a linear stability analysis in the previous section for multiple solutions of the nonlinear steady-state problem (20) subject to (21) concerned symmetric, antisymmetric and general perturbations.

To verify the temporal stability results of suction flows ($R < 0$), we consider only the general perturbations and solve the nonlinear time dependent problem (16) subject to the boundary conditions

$$f(-1) = -1, \quad f(1) = 1, \quad f'(-1) = 0, \quad f'(1) = 0, \tag{31}$$

and initial condition

$$f(y, R, \alpha, 0) = F(y, R, \alpha) + \varphi(y), \tag{32}$$

where F is the symmetric solution of the steady-state problem (20), (28), and

$$\varphi(y) = \varepsilon cos(\omega y + \theta) \tag{33}$$

is a small perturbation for F, ε is the amplitude and ω is the frequency of the perturbation. We can choose different θ for a sinusoidal or a cosine perturbation.

We introduce a new variable $t^* = \frac{R}{2\alpha} ln(1 - \frac{2\alpha t}{R})$ that $0 \leq t^* < \infty$. By substituting t^* into (16) yields the problem

$$-f_{yyt^*} - \frac{1}{R} f_{yyyy} - f f_{yyy} + f_y f_{yy} - \frac{\alpha}{R}(y f_{yyy} + 3 f_{yy}) = 0 \tag{34}$$

with the boundary conditions (31) and initial condition (32).

We solve the problem (34) subject to (31) and (32) by means of a finite difference method again. Let h and τ be the increments of the variables y and t^*. The set of grid points in the y, t^*-plane is given by $y = -1 + jh$, $t^* = n\tau$, where $j = 0, 1, 2, \cdots, 2M$, and $n = 0, 1, 2, \cdots$. The approximation to $f(-1 + jh, n\tau)$ is denoted by f_j^n. Then the finite difference equation approximating the differential equation (34) is

$$-\frac{f_{j+1}^{n+1} - 2f_j^{n+1} + f_{j-1}^{n+1} - f_{j+1}^n + 2f_j^n - f_{j-1}^n}{\tau h^2} - \frac{1}{R}\left(\frac{f_{j+2}^{n+1} - 4f_{j+1}^{n+1} + 6f_j^{n+1} - 4f_{j-1}^{n+1} + f_{j-2}^{n+1}}{h^4}\right)$$
$$-f_j^n\left(\frac{\frac{1}{2}f_{j+2}^n - f_{j+1}^n + f_{j-1}^n - \frac{1}{2}f_{j-2}^n}{h^3}\right) + \left(\frac{f_{j+1}^n - f_{j-1}^n}{2h}\right)\left(\frac{f_{j+1}^n - 2f_j^n + f_{j-1}^n}{h^2}\right)$$
$$-\frac{\alpha}{R}\left((-1+jh)\left(\frac{\frac{1}{2}f_{j+2}^{n+1} - f_{j+1}^{n+1} + f_{j-1}^{n+1} - \frac{1}{2}f_{j-2}^{n+1}}{h^3}\right) + 3\left(\frac{f_{j+1}^{n+1} - 2f_j^{n+1} + f_{j-1}^{n+1}}{h^2}\right)\right) = 0,$$

where $j = 2, \cdots, 2M - 2$, $n = 0, 1, 2, \cdots$. The boundary conditions (31) are

interpreted as

$$
\begin{aligned}
&f_0^{n+1} = -1, \quad f_{2M}^{n+1} = 1, \\
&\frac{-25f_0^{n+1} + 48f_1^{n+1} - 36f_2^{n+1} + 16f_3^{n+1} - 3f_4^{n+1}}{12h} = 0, \\
&\frac{3f_{2M-4}^{n+1} - 16f_{2M-3}^{n+1} + 36f_{2M-2}^{n+1} - 48f_{2M-1}^{n+1} + 25f_{2M}^{n+1}}{12h} = 0, \quad n = 0, 1, 2, \cdots,
\end{aligned}
$$

and the initial condition (32) is interpreted as

$$f_j^0 = F(-1 + jh) + \varphi(-1 + jh). \quad j = 0, \cdots, 2M.$$

This finite difference scheme is of first order in time and of second order in space. Clearly, these equations can be used recursively to determine all the f_j^n for $0 \leq j \leq 2M$, $n \geq 0$. For the simplification of the presentation, we only provide the verification for the stability of the suction flows with a few selected α, e.g. $\alpha = -5$, $-1/2$, $1/2$, 1 and 3. Other cases can all be verified in the same way. Also for convenience, we only show numerical results of above problem under the perturbation $\varphi(y) = 0.0001cos(200y)$ in below figures. We did test it for various ω and θ, and obtain same stability results.

The results of type I solutions with $-5 \leq \alpha \leq 1$ are plotted in Fig. 18. In Figs. 18(a) and 18(b), for the case of $\alpha = -5$, the initial perturbation decays to zero as $t^* \to \infty$ at $R = -14.3$ but not as $t^* \to \infty$ at $R = -14.4$, indicating that the type I solutions at $R = -14.3$ are stable, but unstable at $R = -14.4$. The other cases for $R > -14.3$ and $R < -14.4$ are also examined and the same results are obtained as those at $R = -14.3$ and -14.4, respectively. So we can infer that there is a critical R, above which the solutions are stable and below which the solutions become unstable, between -14.4 and -14.3 with $\alpha = -5$. Similarly, we can obtain that such a R exists between -6.4 and -6.3 with $\alpha = -1/2$ as shown in figs. 18(c) and 18(d), and there is also such a R between -6 and -5.9 with $\alpha = 1/2$ as shown in figs. 18(e) and 18(f). Figs. 18(g) and 18(h) indicate that the type I solutions are stable for $R < 0$ with $\alpha = 1$.

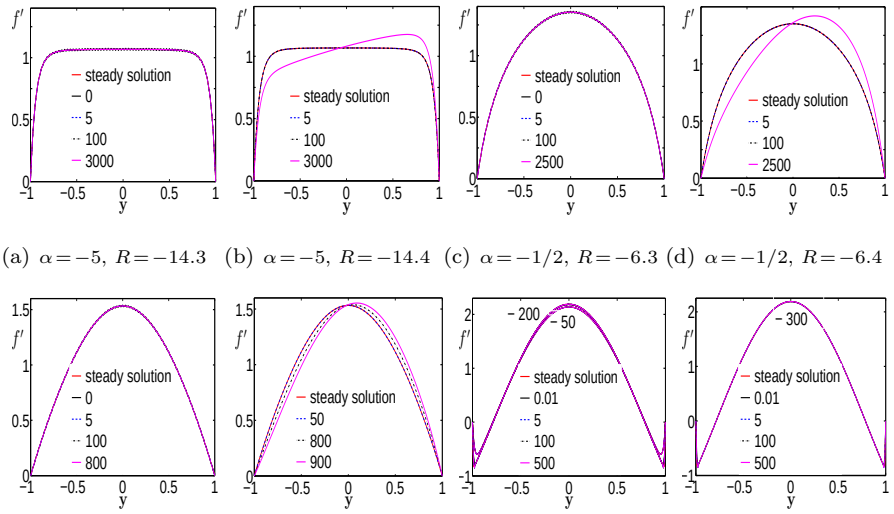

(a) $\alpha=-5$, $R=-14.3$ (b) $\alpha=-5$, $R=-14.4$ (c) $\alpha=-1/2$, $R=-6.3$ (d) $\alpha=-1/2$, $R=-6.4$

(e) $\alpha=1/2$, $R=-5.9$ (f) $\alpha=1/2$, $R=-6$ (g) $\alpha=1$, $R=-50,-200$ (h) $\alpha=1$, $R=-300$

Figure 18: Values of $f'(y,t^*)$ at different times and $F'(y)$ of the type I solutions with a few suction cross-flow Reynolds numbers R and wall expansion ratios α.

For the type II solutions with $-5 \leq \alpha \leq 1$, we have chosen the cross-flow Reynolds numbers for which these solutions exist, and the results are shown in Fig. 19. In Fig. 19(a), for $\alpha = -5$, we observe that the small perturbation for the type II solutions at $R = -14.5$ is propagating away from zero as $t^* \to \infty$. We have examined the situations at other cross-flow Reynolds numbers and obtained same results. So that the type II solutions with $\alpha = -5$ are unstable. Similarly, we can obtain that the type II solutions with $\alpha = \pm 1/2$ and 1 are also unstable. For the type III solutions with $-5 \leq \alpha \leq 1$, the numerical results with a few R are plotted in Fig. 20, and the same phenomenon as type II solutions are obtained. We have also considered the other cases of R. Consequently, the type III solutions with $-5 \leq \alpha \leq 1$ are always unstable.

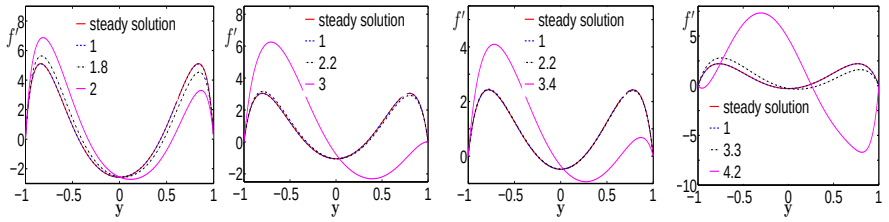

(a) $\alpha=-5$, $R=-14.5$ (b) $\alpha=-1/2$, $R=-12.6$ (c) $\alpha=1/2$, $R=-11.8$ (d) $\alpha=1$, $R=-11.3$

Figure 19: Values of $f'(y,t^*)$ at different times and $F'(y)$ of the type II solutions with a few R and α.

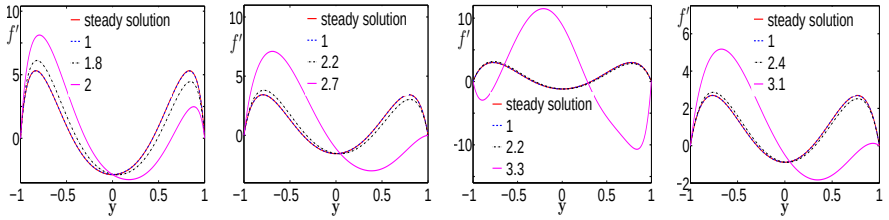

(a) $\alpha=-5$, $R=-14.5$ (b) $\alpha=-1/2$, $R=-12.6$ (c) $\alpha=1/2$, $R=-11.8$ (d) $\alpha=1$, $R=-11.3$

Figure 20: Values of $f'(y,t^*)$ at different times and $F'(y)$ of the type III solutions with a few R and α.

When $\alpha = 3$, in Fig. 21(a), we can obtain that the type I solutions at $R = -0.1$ and -4.2 are stable. Additionally, we test the other R and obtain same results. So that the solutions of type I are stable. For other solutions, in Figs. 21(b)-21(d), it can be clearly seen that the type IV solutions at $R = -0.8$ are unstable, and the types II and III solutions at $R = -9.6$ are also unstable. We also test the other R and obtain same results, indicating that the types II, III and IV solutions with $\alpha = 3$ are unstable.

These results are consistent with those obtained in section 4. It seems that the linear stability analysis for small perturbations is very effective in this flow problem.

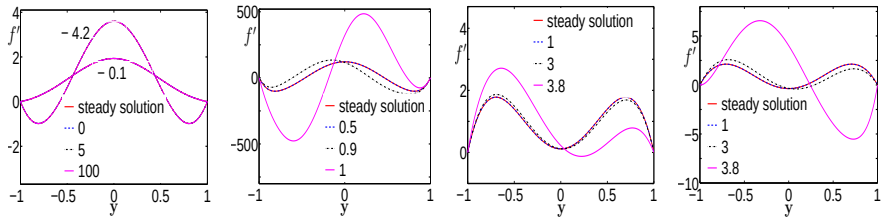

(a) $\alpha=3$, $R=-0.1,-4.2$ (b) $\alpha=3$, $R=-0.8$ (c) $\alpha=3$, $R=-9.6$ (d) $\alpha=3$, $R=-9.6$

Figure 21: Values of $f'(y,t^*)$ at different times and $F'(y)$ of the solutions of (a) type I, $R=-0.1$ and -4.2, (b) type IV, $R=-0.8$, (c) type II, $R=-9.6$ and (d) type III, $R=-9.6$; $\alpha=3$.

6. Conclusion

In this numerical study, a flow problem occurring in a uniformly porous channel with moving walls is considered. We calculate multiple similarity solutions for the Navier-Stokes equations of this problem when the expansion ratio α is in the range of $[-5,3]$, and analyse the temporal stability of these solutions under symmetric, antisymmetric and general perturbations. On one hand, we use the linear eigenvalue analysis method to provide the ranges of the cross-flow Reynolds number R where these solutions are stable. For the type I solutions with $-5\leq\alpha\leq 1/2$, there is an interval of R which becomes smaller and smaller as the value of α increases in which the solutions are stable, and the instability of these solutions is determined by the antisymmetric perturbations. Meanwhile, the type I solutions with $1\leq\alpha\leq 3$ are always stable in all R where they exist. So the expansion ratio α has a great influence on the temporal stability of these solutions. Other types of solutions with $-5\leq\alpha\leq 3$ whose axial velocity profiles have an inflection point are always unstable, suggesting that these solutions may transition to turbulence prior to physically attaining these shapes. In other words, these solutions may not be physically observed. The instability of type IV solutions with $\alpha=3$ is determined by the symmetric perturbations, while the instability of type III solutions with $-5\leq\alpha\leq 3$ is determined by the antisymmetric perturbations. So antisymmetric perturbations seem to be more

decisive for stability in most cases.

On the other hand, we provide some validation of the linear stability results by directly solving the original time dependent nonlinear partial differential equation with an initial perturbation. The computational results agree well with those obtained from the linear stability analysis.

It should be noted that all the perturbations we have considered are constrained in the space of self-similar solutions, and direct simulations of Navier-Stokes equations would be needed to further validate our results.

Acknowledgements

This work is partially supported by the National Natural Science Foundation of China (Nos. 11771040 and 11861131004) and the Fundamental Research Funds for the Central Universities (No. 06500073).

References

[1] E. Dauenhauer, J. Majdalani, Exact self-similarity solution of the navier-stokes equations for a porous channel with orthogonally moving walls, Physics of Fluids 15 (6) (2003) 1485–1495. doi:10.1063/1.1567719.

[2] J. Majdalani, C. Zhou, C. Dawson, Two-dimensional viscous flow between slowly expanding or contracting walls with weak permeability, Journal of Biomechanics 35 (10) (2002) 1399–1403. doi:10.1016/S0021-9290(02)00186-0.

[3] J. Majdalani, C. Zhou, Moderate-to-large injection and suction driven channel flows with expanding or contracting walls, ZAMM - Journal of Applied Mathematics and Mechanics / Zeitschrift fr Angewandte Mathematik und Mechanik 83 (3) (2003) 181–196. doi:10.1002/zamm.200310018.

[4] C. Zhou, J. Majdalani, Improved mean-flow solution for slab rocket motors with regressing walls, Journal of Propulsion and Power 18 (3) (2002) 703–711. doi:10.2514/2.5987.

[5] H. Xu, Z.-L. Lin, S.-J. Liao, J.-Z. Wu, J. Majdalani, Homotopy based solutions of the navier-stokes equations for a porous channel with orthogonally moving walls, Physics of Fluids 22 (5) (2010) 053601. doi:10.1063/1.3392770.

[6] J. Brady, A. Acrivos, Steady flow in a channel or tube with an accelerating surface velocity. an exact solution to the navier-stokes equations with reverse flow, Journal of Fluid Mechanics 112 (1981) 127–150. doi:10.1017/S0022112081000323.

[7] J. Brady, A. Acrivos, Closed-cavity laminar flows at moderate reynolds numbers, Journal of Fluid Mechanics 115 (1982) 427–442. doi:10.1017/S0022112082000834.

[8] L. Durlofsky, J. Brady, The spatial stability of a class of similarity solutions, Physics of Fluids 27 (5) (1984) 1068–1076. doi:10.1063/1.864736.

[9] S. Ferro, G. Gnavi, Spatial stability of similarity solutions for viscous flows in channels with porous walls, Physics of Fluids 12 (4) (2000) 797–802. doi:10.1063/1.870336.

[10] M. Zaturska, P. Drazin, W. Banks, On the flow of a viscous fluid driven along a channel by suction at porous walls, Fluid Dynamics Research 4 (3) (1988) 151–178.

[11] S. Uchida, H. Aoki, Unsteady flows in a semi-infinite contracting or expanding pipe, Journal of Fluid Mechanics 82 (2) (1977) 371–387. doi:10.1017/S0022112077000718.

[12] A. S. Berman, Laminar flow in channels with porous walls, Journal of Applied Physics 24 (9) (1953) 1232–1235. doi:10.1063/1.1721476.